

Energy-Efficient p-Bit-Based Fully-Connected Quantum-Inspired Simulated Annealer with Dual BRAM Architecture

Naoya Onizawa¹, Taiga Kubuta¹, Duckgyu Shin¹, and Takahiro Hanyu¹

¹Research Institute of Electrical Communication, Tohoku University, Sendai 980-8577, Japan

Emails: naoya.onizawa.a7@tohoku.ac.jp, ryoma.sasaki.p6@dc.tohoku.ac.jp, duckgyu.shin.p4@dc.tohoku.ac.jp, takahiro.hanyu.c4@tohoku.ac.jp

Abstract

Probabilistic bits (p-bits) offer an energy-efficient hardware abstraction for stochastic optimization; however, existing p-bit-based simulated annealing accelerators suffer from poor scalability and limited support for fully connected graphs due to fan-out and memory overhead. This paper presents an energy-efficient FPGA architecture for stochastic simulated quantum annealing (SSQA) that addresses these challenges. The proposed design combines a spin-serial and replica-parallel update schedule with a dual-BRAM delay-line architecture, enabling scalable support for fully connected Ising models while eliminating fan-out growth in logic resources. By exploiting SSQA, the architecture achieves fast convergence using only final replica states, significantly reducing memory requirements compared to conventional p-bit-based annealers. Implemented on a Xilinx ZC706 FPGA, the proposed system solves an 800-node MAX-CUT benchmark and achieves up to 50% reduction in energy consumption and over 90% reduction in logic resources compared with prior FPGA-based p-bit annealing architectures. These results demonstrate the practicality of quantum-inspired, p-bit-based annealing hardware for large-scale combinatorial optimization under strict energy and resource constraints.

Keywords: Combinatorial optimization, Hamiltonian, Ising model, simulated annealing, stochastic computing, FPGA

1 INTRODUCTION

In recent years, probabilistic bits (p-bits) have emerged as a compact hardware abstraction for stochastic inference and optimization [1]. Leveraging embedded magnetic tunnel junctions [2–4], p-bits offer tunable randomness and sub-nanosecond switching, enabling energy-efficient realization of algorithms such as Boltzmann machines [5], invertible logic [6], Bayesian inference [7], and Gibbs sampling [8].

A key application of p-bits is simulated annealing (SA) for combinatorial optimization [9, 10]. Existing stochastic-computing SA accelerators (SSA) implement time-multiplexed arithmetic with FPGA-friendly circuitry [11–14] but exhibit two critical limitations: (i) spin-parallel datapaths do not scale beyond nearest-neighbor graphs, and (ii) shift-register-based delay lines cause logic and routing cost to grow linearly with the number of spins [15, 16]. These constraints limit the practicality of p-bit-based annealers for dense or fully connected problems despite their algorithmic potential.

This paper introduces a fully connected, energy-efficient stochastic simulated quantum annealing (SSQA) engine that addresses both limitations. The proposed architecture integrates a dual-BRAM delay-line scheme with replica-parallel/spin-serial scheduling to eliminate the $O(N)$ fan-out associated with prior shift-register-based implementations while retaining the proven spin-gate formulation from [16]. Centralizing delays in BRAM keeps LUT and FF usage nearly constant as the spin count increases. Implemented on a Xilinx ZC706, the system solves 800-node MAX-CUT benchmarks while sustaining the energy and resource advantages required for embedded deployment.

The contributions of this paper are threefold: (1) A refined SSQA hardware platform that adapts the existing spin-gate circuit to a spin-serial schedule while preserving fully connected graph support and bounding the per-spin compute cost to $N+1$ cycles; (2) A novel dual-BRAM delay-line architecture that eliminates the fan-out and routing bottlenecks of prior SSA/SSQA accelerators, leading to flat LUT/FF scaling with the number of spins; (3) A comprehensive evaluation across hardware prototypes and software baselines, including new sensitivity analyses and application case studies, demonstrating substantial improvements in energy, resource usage, and solution quality.

The remainder of the paper is organized as follows. Section 2 reviews SSQA and summarizes related annealing hardware. Section 3 details the proposed architecture. Section 4 reports algorithmic and hardware evaluations, including extended benchmarks. Section 5 analyzes trade-offs and broader implications, and Section 6 concludes the paper.

2 PRELIMINARIES

2.1 p-bit-based simulated annealing for Ising model

A new device model, known as the p-bit, has been proposed [1]. This probabilistic nature makes p-bits a valuable tool for solving certain types of problems that require a degree of randomness or uncertainty. The output state of a p-bit is represented as follows:

$$\sigma_i(t+1) = \text{sgn}\left(r_i(t) + \tanh(I_i(t+1))\right), \quad (1)$$

where $\sigma_i(t+1) \in \{-1, 1\}$ is a binary output signal, $I_i(t+1)$ is a real-valued input signal, and $r_i(t) \in \{-1 : 1\}$ is a random signal.

p-bit-based simulated annealing (pSA) for Ising models [18] has been reported as one of the applications of p-bits [9]. In pSA, each p-bit is biased by h and connected to other p-bits through weights J forming a spin network. In this context, a p-bit acts as a classical stochastic spin, taking on values of $+1$ or -1 with probabilities determined by its input. This spin network is based on the Ising model, which represents the Hamiltonian (energy function) as follows:

$$H(\sigma) = - \sum_i h_i \sigma_i - \sum_{i < j} J_{ij} \sigma_i \sigma_j. \quad (2)$$

where i and j ($1 \leq i, j \leq N$) are indices of p-bits, and N is the number of p-bits. The spins in the Ising spin network are implemented using p-bits. The input of p-bit $I_i(t+1)$ is calculated using the outputs of other p-bits as defined below:

$$I_i(t+1) = I_0 \left(h_i + \sum_j J_{ij} \cdot \sigma_j(t) \right), \quad (3)$$

where I_0 is a pseudo inverse temperature used to control the simulated annealing.

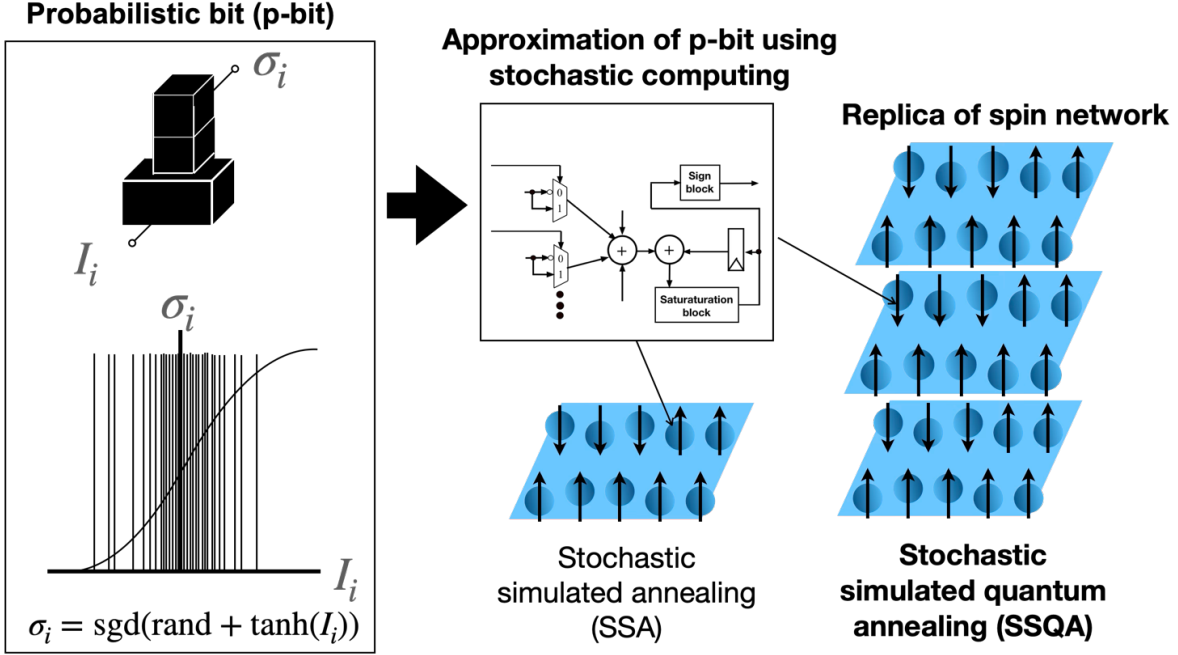


Figure 1: Variation of p-bit-based simulated annealing. Stochastic simulated annealing (SSA) [17] is a p-bit-based simulated annealing (SA) method approximated using stochastic computing. Stochastic simulated quantum annealing (SSQA) [17] is an alternative p-bit-based SA approach that utilizes replicas of a spin network to mimic quantum annealing on a classical computer.

pSA is approximated using stochastic computing, known as stochastic simulated annealing (SSA) [17], as shown in Fig. 1. Stochastic computing (SC) is a computational paradigm that represents numbers as streams of stochastic bit sequences, allowing arithmetic operations to be performed using simple logic gates [11, 12]. Unlike conventional binary computation, SC leverages probability and randomness to achieve low-cost, fault-tolerant, and energy-efficient computing [19–22]. In SSA, Eqs. (1) and (3) are approximated using SC, which can be implemented in digital circuits.

2.2 Stochastic simulated quantum annealing (SSQA)

Stochastic simulated quantum annealing (SSQA) is an alternative p-bit-based SA approach that utilizes replicas of a spin network to mimic quantum annealing on a classical computer [17]. Fig. 2 illustrates a SSQA spin network, which consists of R replicas. Each replica consists of N p-bits based on the Ising model, and adjacent layers are connected through interaction coefficients Q . The SSQA spin network is represented by a pseudo quantum Hamiltonian, which is approximated by The Trotter-Suzuki decomposition from the quantum Hamiltonian [23, 24]. This allows its representation using multiple replicas of spin network on classical computers, thereby approximating and representing the time evolution of QA. The pseudo quantum Hamiltonian, denoted $H_c(\sigma)$, can be expressed as follows:

$$H_c(\sigma) = \sum_{k=1}^R \left(H_p(\sigma) - Q \sum_i \sigma_{i,k} \sigma_{i,k+1} \right), \quad (4)$$

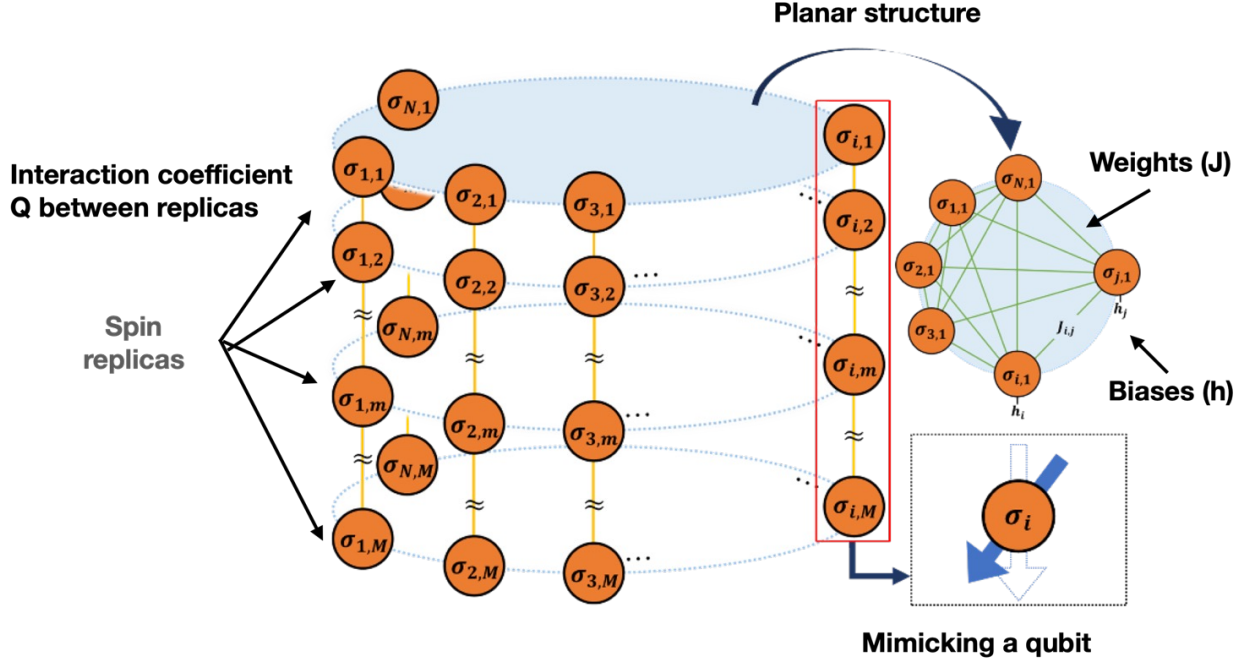


Figure 2: An SSQA spin network consisting of $N \times R$ p-bits, where each replica consists of N p-bits. Each replica of the spin network is based on the Ising model, and adjacent layers are connected through interaction coefficients Q .

$$H_p(\sigma) = - \sum_i h_i \sigma_{i,k} - \sum_{i < j} J_{ij} \sigma_{i,k} \sigma_{j,k}, \quad (5)$$

where $H_p(\sigma)$ is the problem Hamiltonian, $\sigma_{i,k}$ represents the spin state of the k -th replica of the spin network ($1 \leq k \leq R$), R is the number of replicas of spins used to represent the q-bit, and Q is a scheduling parameter corresponding to Γ_x . The problem Hamiltonian, $H_p(\sigma)$, is the same as the one in (Eq. (2)) used in SA.

The spin-update algorithm of SSQA is designed based on stochastic computing as SSQA is an extension of SSA. The update algorithm for the i -th spin in the k -th replica is as follows:

$$\begin{aligned} I_{i,k}(t+1) &= h_i + \sum_j J_{ij} \cdot \sigma_{j,k}(t) + n_{rnd} \cdot r_i(t) \\ &+ Q(t) \cdot \sigma_{i,k+1}(t-d), \end{aligned} \quad (6a)$$

$$I_{s,i,k}(t+1) = \begin{cases} I_0 - \alpha, & \text{if } I_{s,i,k}(t) + I_{i,k}(t+1) \geq I_0 \\ -I_0, & \text{else if } I_{s,i,k}(t) + I_{i,k}(t+1) < -I_0 \\ I_{s,i,k}(t) + I_{i,k}(t+1), & \text{otherwise} \end{cases} \quad (6b)$$

$$\sigma_{i,k}(t+1) = \begin{cases} 1, & \text{if } I_{s,i,k}(t+1) \geq 0 \\ -1, & \text{otherwise.} \end{cases} \quad (6c)$$

where $\sigma_{i,k}(t) \in \{-1, 1\}$ and $\sigma_{i,k}(t+1) \in \{-1, 1\}$ represent the binary input and output spin states, respectively. Here, $\sigma_{i,k+1}(t-d)$ represents the i -th spin state in the $(k+1)$ -th replica, and d is the delay cycle for the coupled effect. Note that $d = 1$ is used in this paper. α is a design parameter that defines the offset of the saturation threshold in stochastic computing, and is fixed

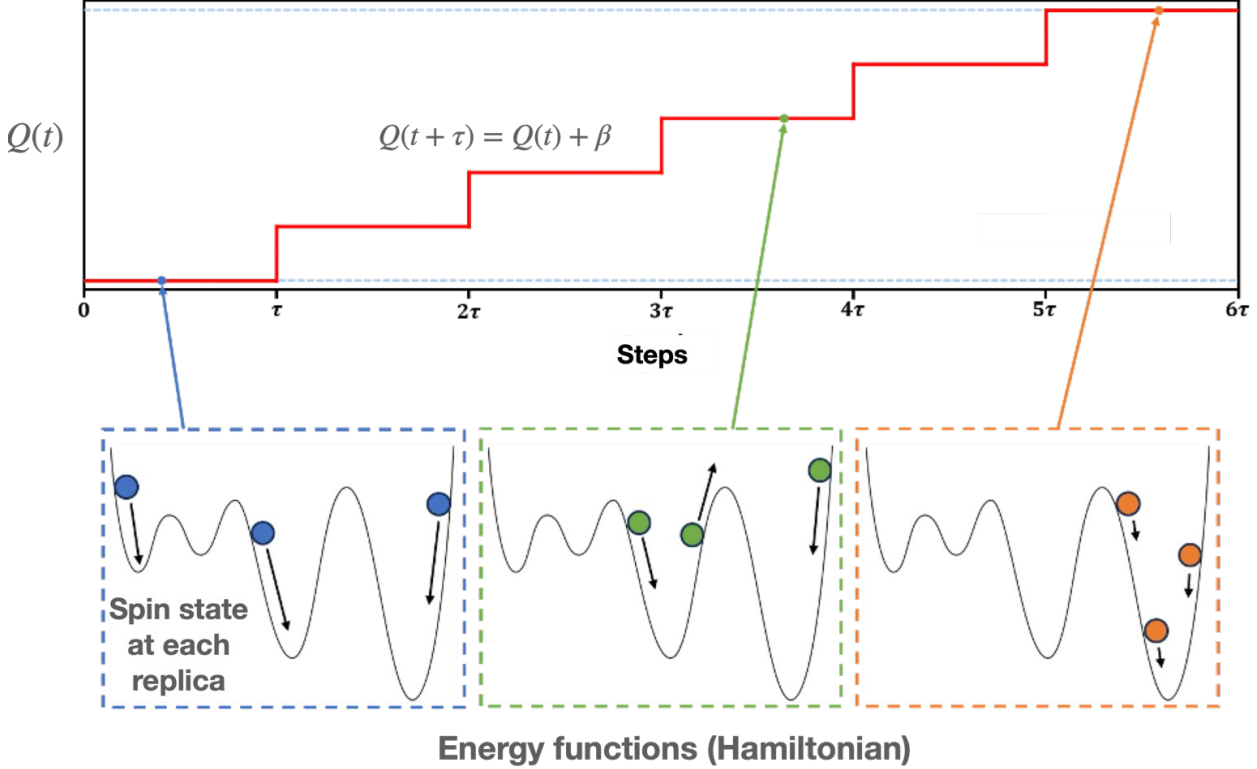


Figure 3: Evolution of the interaction constant $Q(t)$ over the annealing steps in the SSQA method, illustrating how the coupling strength between replicas is gradually increased. The optimization process is guided by this schedule: low $Q(t)$ values allow independent exploration within each replica, while higher $Q(t)$ values enhance inter-replica coupling, encouraging convergence toward the global minimum of the energy function H . This mechanism enables efficient solution search via quantum-inspired tunneling behavior.

to 1 throughout the annealing process. The coupled effect from the upper replica is represented by $Q(t) \cdot \sigma_{i,k+1}(t - d)$. $I_{i,k}(t + 1)$ and $Is_{i,k}(t + 1)$ are real-valued internal signals. In stochastic computing, Eq. (6b) and Eq. (6c) approximate $\tanh(I_0 \cdot I_{i,k})$ [12, 22], where $Is_{i,k}$ is the input of Eq. (6c). The mean of $\sigma_{i,k}$ is closer to the output of the \tanh function as stochastic computing is used to approximate \tanh of the p-bit equation.

The SSQA method controls the probability of spin state updates through the interaction constant $Q(t)$ between networks. Fig. 3 represents the interaction constant $Q(t)$ for the annealing step t in the SSQA method. $Q(t)$ increases from its minimum value Q_{\min} to its maximum value Q_{\max} according to the following equation:

$$Q(t + \tau) = Q(t) + \beta, \quad (7)$$

where τ is the number of annealing steps during which the interaction constant remains constant, and β is the increment of the interaction constant.

When Q is small, the spin network is loosely coupled to the upper and lower replicas, allowing each replica to explore the minimum value of the problem's energy function independently while minimizing the influence from adjacent replicas. On the other hand, when Q is large, the spin network becomes tightly coupled, enabling it to reach the minimum value by leveraging spin replicas with low energy.

Table 1: Feature comparison of representative FPGA annealers.

Design	Update topology	Connectivity	Delay storage	
HA-SSA [15]	Spin parallel	Four-neighbor lattice	Distributed shift registers	Routing
IPAPT [25]	Spin parallel	Four-neighbor lattice	Distributed shift registers	Replica
PYNQ SSQA [16]	Replica parallel / spin serial	Sparse graphs	Shift registers per replica	
This work	Replica parallel / spin serial	Fully connected	Dual BRAM delay line	Fan-out a

2.3 Related Work

Early FPGA realizations of simulated annealing employed spin-parallel datapaths with localized shift registers to cache intermediate states [15, 25]. These designs excel at nearest-neighbor Ising problems but require $O(N)$ multiplexers and incur large routing fan-out, which prevents them from scaling to dense graphs or replica-based algorithms. More recent SSQA prototypes on PYNQ boards [16] introduced replica parallelism but retained distributed delay elements, so resource usage still grows with the spin count.

Table 1 contrasts representative accelerators with the proposed platform. The prior HA-SSA and IPAPT architectures share a spin-parallel organization: HA-SSA leverages stochastic computing to reduce arithmetic complexity, whereas IPAPT instead employs parallel tempering, and both offer limited connectivity and store multiple intermediate replicas, leading to large memory footprints. In contrast, our design centralizes the delay line in dual BRAMs, enabling constant fan-out, single-replica storage, and full-graph programmability.

3 SPIN-SERIAL/REPLICA-PARALLEL HARDWARE ARCHITECTURE FOR SSQA

3.1 Overall Structure

Fig. 4 illustrates the proposed hardware architecture designed for implementing the SSQA algorithm described by Eq. (6c). The architecture supports a fully connected Ising model comprising N spins and executes computations across R replicas. It employs a spin-serial and replica-parallel approach. The spin-serial structure significantly reduces the wiring complexity compared to a spin-parallel implementation. In a spin-parallel approach, all spin updates are performed simultaneously, requiring each spin gate to access the states of all other spins at once. As a result, each spin gate must incorporate N multiplexers or equivalent routing logic to select and process weighted inputs from the other N spins, leading to increased wiring complexity. To minimize hardware complexity, this design adopts serial computation, performing spin interactions sequentially in a time-multiplexed manner. The replica-parallel structure optimizes memory efficiency, allowing multiple replicas to concurrently access the shared weight matrix J . This concurrent access reduces the frequency of memory reads and thus enhances performance. The proposed architecture consists of the following key components: a spin gate array for computation, BRAM for storing the weight matrix J , an XOR-shift random number generator, and a scheduler module responsible for overall control. Throughout this paper we refer to Xilinx block RAM macros as BRAMs (denoted by the symbol B in the schematics), emphasizing that they are dual-port memories with fixed granularity rather than generic flip-flop arrays.

The spin gate array comprises R identical spin gate circuits and a delay circuit. Fig. 5 shows the detailed structure of a single spin gate circuit. Following the formulation in [16], each spin gate

retains the established stochastic-computing datapath; our contribution is to embed that circuit within a spin-serial scheduler so that a single multiplexer suffices regardless of the number of spin connections. During each clock cycle, due to the spin-serial design, the output of a specific spin and the associated weight J_{ij} are retrieved from BRAM to compute Eq. (6a). Repeating this for N clock cycles completes the interaction computations for all connections of one spin. An additional clock cycle computes Eqs. (6b) and (6c), finalizing the update for one spin. This procedure repeats for all N spins, constituting one complete update step as defined by Eq. (6c). As Eq. (6a) requires data from three consecutive time steps ($t+1$, t , and $t-1$), a delay circuit retains this necessary data. Two delay circuit implementations are evaluated, with detailed explanations provided in subsequent sections.

Besides spin interactions, the SSQA algorithm requires the generation of various signals, including inverse temperature, random signals and their magnitudes, and interactions between spin networks. Random signals $r_{i,k}(t)$ are produced by the XOR-shift random number generator [26]. A 64-bit XOR-shift generator is designed to generate R -parallel random signals at each clock cycle. The inverse temperature I_0 and interaction coefficient $Q(t)$ are generated by the scheduler module. The scheduler module also coordinates the entire circuit operation, including managing input/output processes, enabling, and resetting components. Since hyperparameters influence interaction coefficients and overall control, the scheduler receives these hyperparameters via AXI communication from a CPU integrated into the Zynq FPGA.

3.2 Shift Register-Based Delay Circuit

Fig. 6 (a) shows the shift register-based delay circuit used for managing spin states in the k -th replicated spin gate [16]. Each spin gate computation requires spin states from three consecutive time steps ($t+1$, t , and $t-1$), as described by Eq. (6c). Therefore, the delay circuit consists of three sequential register blocks, each containing N registers corresponding to these three time steps.

The operation of each register stage is described as follows:

- **First-stage block** stores newly computed spin states $\sigma_{i,k}(t+1)$ sequentially, shifting data by one register per spin computation. The shift operations are controlled by signals (en_1 , en_2) generated by the scheduler.
- **Second-stage block** retains spin states delayed by one annealing step, $\sigma_{i,k}(t)$. After each annealing step, all N spin states computed during the step are simultaneously loaded into this block. During the next annealing step, the block shifts once per spin interaction calculation, providing the appropriate delayed state $\sigma_{i,k}(t)$ sequentially for computation.
- **Third-stage block** retains spin states delayed by two annealing steps, $\sigma_{i,k}(t-1)$, and provides them during spin network interaction calculations $Q(t) \cdot \sigma_{i,k+1}(t-1)$. The states from the second-stage block are transferred simultaneously into this block at each annealing step boundary, and subsequently shifted sequentially during interaction calculations.

Similarly, Fig. 6 (b) illustrates the delay circuit designed for the saturated internal signals $Is_{i,k}$ within the same replicated spin gate.

While straightforward, the shift register-based delay circuit faces scalability challenges. The circuit requires $3N$ registers, resulting in linear hardware area growth with respect to N . Moreover, the fan-out of the control signals also grows with N , leading to linear increases in FPGA area due to increased routing complexity. To overcome these scalability limitations, we propose an alternative dual BRAM-based delay circuit, detailed in the subsequent subsection.

3.3 Dual BRAM-Based Delay Circuit

Fig. 7 (a) illustrates the dual BRAM-based delay circuit for storing spin states of the k -th replicated spin gate. Fig. 7 (b) depicts a similar delay circuit for saturated internal signals $Is_{i,k}$. Two BRAM blocks alternate operation via a multiplexer at each annealing step, providing delays of one and two annealing steps. Unlike shift register-based designs, where fan-out problems worsen as the number of spins increases, the proposed dual BRAM-based structure significantly mitigates this issue. BRAM’s centralized addressing capability reduces high fan-out wiring, enhancing scalability with increasing spin counts. At the same time, relying on coarse-grained BRAM macros introduces practical trade-offs: unused capacity leads to fragmentation in small-scale instances, only two memory ports are available per block, and the total replica count is ultimately limited by the number of BRAM tiles on the target FPGA. We therefore co-design the scheduler and memory map to avoid read/write contention and report the resulting utilization in Section 4.

The dual BRAM-based delay circuit operates as follows:

- During annealing step $t + 1$ ($t = 2n$), newly computed spin states $\sigma_{i,k}(t + 1)$ are written to BRAM1 using write address $addra1$ and write enable signal $ena1$, activated at spin update timing ($enupd$). Conversely, during step $t = 2n - 1$, states are written to BRAM2 using $addra2$ and $ena2$.
- For reading states during step t , BRAM1 outputs stored states $\sigma_{i,k}(t)$, accessed via read address $addrb1$ corresponding to spin interaction index ($countbit$). During step $t = 2n - 1$, BRAM2 provides $\sigma_{i,k}(t)$ using $addrb2$.
- At step $t - 1$ ($t = 2n$), BRAM1 outputs $\sigma_{i,k}(t - 1)$ for replica interaction calculations, with read address set to $countspin$. Similarly, at $t = 2n - 1$, BRAM2 outputs $\sigma_{i,k}(t - 1)$ using the same addressing scheme.

Since BRAM inherently performs read operations before writes when accessing the same address simultaneously, the integrity of spin state data is preserved during each annealing step.

4 EVALUATION

4.1 Experimental setup

All software evaluations were executed with an Intel Core-7 7800X (6 cores) and 64 GB of DDR5 memory for the CPU baseline, and an Intel Xeon Gold 6430 (32 cores, AVX-512 enabled), 128 GB of DDR5 memory, and an NVIDIA RTX 4090 GPU for the accelerator experiments. The CPU baseline uses Python 3.6.8 implementations, and the GPU baseline is built with PyCUDA [27] 2022.1 and CUDA 12.2/nvcc 12.2. We fixed the pseudo-random seeds to ensure reproducibility across back-ends.

The G-set benchmarks [28] were used to sweep the number of SSQA replicas R and annealing steps; additional combinatorial optimization instances are introduced in Section 5.2. The FPGA design was authored in SystemVerilog, synthesized and placed using Vivado 2023.2 targeting the Xilinx ZC706 board, and validated for functional equivalence to the software reference. Power estimates rely on Vivado’s vector-less analysis with activity factors derived from post-implementation simulation.

Table 2: Summary of MAX-CUT problems used for evaluation.

Graph	# nodes	Structure	Weights (J_{ij})	# edges ($J_{ij} \neq 0$)	Best value
G11	800	toroidal	{+1, -1}	1600	564
G12	800	toroidal	{+1, -1}	1600	566
G13	800	toroidal	{+1, -1}	1600	582
G14	800	planar	{+1}	4694	3064
G15	800	planar	{+1}	4661	3050

4.2 Algorithm evaluation

Table 2 summarizes the benchmarks for the MAX-CUT problems that are used for evaluation. The Gset includes the Gx graphs with different shapes, and weights [28]. Fig. 8 (a) illustrates the relationship between the average cut value and the number of layers, R , for the SSQA algorithm, focusing on the G11 instance from the G-set. Each simulation is conducted according to the following procedure. First, the SSQA algorithm is executed for a predefined number of annealing steps. In this process, R replicas of N -spin configurations are evolved in parallel. After the annealing process, the configuration yielding the highest cut value among the R replicas is selected as the final solution. Each reported value is the average of 100 independent simulation runs, with the number of simulation steps varied from 100 to 1000 in increments of 100. The figure clearly demonstrates that the average cut value saturates beyond 15 layers. Additionally, Fig. 8 (b) presents the relationship between the average cut value and the number of simulation steps for various layer counts ranging from 5 to 30. The results confirm that saturation in performance is achieved with 20 or more layers.

Figure 9 extends the replica sweep to all five graphs in Table 2, fixing the annealing steps to 500 while varying R from 1 to 30. Each point aggregates 100 independent trials and is normalized by the best-known cut value. The toroidal (G11–G13) and dense planar (G14–G15) instances all converge within 0.5% of the optimum once $R \geq 20$, indicating that the replica budget selected on G11 generalizes to both sparse and dense connectivity patterns. Based on these observations we adopt $R = 20$ for the hardware implementation, while prior SSQA deployments on graph isomorphism report optimal performance at $R = 25$ [17], highlighting that the best replica count depends on problem structure.

4.3 Shift register vs. dual BRAM

We evaluated the SSQA hardware by comparing two types of delay circuits: one based on shift registers [16] and the other based on dual BRAMs. Both hardware implementations, each with varying numbers of spins, were designed to operate at a target clock frequency of 100 MHz. Fig. 10 (a) illustrates the relationship between the number of LUTs and the number of spins. Due to the spin-serial architecture adopted by the proposed SSQA hardware, the LUT count remains nearly constant for the dual-BRAM-based delay circuit, irrespective of the number of spins. Conversely, for the shift-register-based circuit, the LUT count grows proportionally with the number of spins. This increase is primarily due to the expanded fan-out of control signals for the shift registers, necessitating additional buffering elements such as BUFS. Fig. 10 (b) presents the number of flip-flops (FFs) as a function of the number of spins. For the shift-register-based implementation, the FF count rises linearly with the number of spins, as the size of the delay circuit directly scales with N . On the other hand, the dual-BRAM-based delay circuit does not incorporate FFs, thus maintaining an almost constant FF count regardless of spin count. Fig. 10 (c) shows the number of BRAM

Table 3: Resource utilization of SSQA algorithm on Xilinx ZC706 with 166 MHz for 800 spins.

	Conventional [16] (Shift register)	Proposed (Dual BRAM)
LUT	28,525 (13.1%)	3,170 (1.45%)
FF	50,668 (11.6%)	1,643 (0.38%)
BRAM	78.5 (14.4%)	108.5 (19.9%)
Power [W]	0.306	0.091

Table 4: Performance comparison of SSQA implementations for 800 spins.

	Specification	Clock frequency	Power dissipation
CPU	Core-7 7800X	3400 MHz	140 W
GPU	NVIDIA RTX4090	2235 MHz	450 W
Conventional [16]	Xilinx ZC706	166 MHz	0.306 W
Proposed	Xilinx ZC706	166 MHz	0.091 W

blocks relative to the number of spins. The number of BRAM blocks scales proportionally to N^2 , since the BRAM stores the weight matrix J with size N^2 . Consequently, the dual-BRAM-based implementation requires more BRAM blocks than the shift-register-based approach, as BRAMs are additionally used within the delay circuit. Fig. 10 (d) illustrates the power consumption as a function of the number of spins. The shift-register-based implementation’s power consumption grows proportionally with spin count due to the linear increase in LUT and FF usage. In contrast, the dual-BRAM-based implementation maintains nearly constant power consumption, independent of the number of spins.

Table 3 summarizes the hardware comparison for $N = 800$. Both implementations were designed and evaluated at a frequency of 166 MHz. The proposed dual-BRAM-based architecture achieved an 89% reduction in LUT usage, a 97% reduction in FF usage, and a 70% reduction in power consumption compared to the shift-register-based design. The increase from 78.5 to 108.5 BRAM blocks is a deliberate trade-off: replacing distributed shift registers with two central BRAMs removes the $O(N)$ fan-out without exceeding 20% of ZC706.

4.4 Hardware comparisons

Table 4 summarizes the performance comparison between the SSQA hardware and its CPU and GPU counterparts. The latency per annealing step is fixed by the spin-serial schedule: each spin processes the k incident weights and one update, so the total cycles per step are $N \times (k + 1)$. For the G-set graphs G11–G13 ($k = 4$), one step spans 800×5 cycles; fully connected instances with $k = N - 1$ scale accordingly. When a graph is sparse, the scheduler bypasses zero-weight placeholders in BRAM, eliminating unnecessary reads and reducing the cycle count while keeping

Table 5: Performance comparison between a conventional p-bit based hardware [15] and the proposed SSQA-based hardware.

Graph	HA-SSA [15]				Proposed			
	Best cut value	Average	Memory for spin states	Annealing steps	Best cut value	Average	Memory for spin states	Annealing steps
G11	564	557			564	558		
G12	554	546	13.2 Mb	90,000	554	549	32 kb	500
G13	576	570			578	573		

Table 6: Performance comparisons of FPGA implementation for G11.

	Proposed	HA-SSA [15]	IPAPT [25]
Hardware architecture	Spin serial	Spin parallel	Spin parallel
Graph support	Fully connected	Limited to 4 neighbors	Limited to 4 neighbors
Number of connections per spin	up to 799	4	4
Bit width of h and J supported	4	4	2
FPGA	Xilinx ZC706	Digilent Genesys 2	Vertex-5 (XC5VLX330T)
Clock frequency	166 MHz	100 MHz	150 MHz
Power dissipation	0.091 W	2.138 W	N/A
Annealing latency	12.01 ms	1 ms	2.64 ms
Energy	1.093 mJ	2.138 mJ	N/A
Mean cut value	558.4	558	561
LUT	3,170 (1.45 %)	105,294 (51.7 %)	46,753 (22.5 %)
FF	1,643 (0.38 %)	13,692 (3.36 %)	19,797 (9.55 %)
BRAM blocks	108.5 (19.9 %)	356 (79.9 %)	N/A

the timing model explicit.

Fig. 11 illustrates the trade-off between energy and latency for SSQA implementations in G12 and G15, with the number of steps fixed at 500. In G12, the proposed dual-BRAM-based hardware achieves a 97% reduction in latency and a 99.998% reduction in energy consumption compared to the CPU implementation. When compared with the GPU implementation, it achieves a 70% latency reduction and a 99.994% energy reduction. Due to the increased connectivity in G15 compared to G12, both the latency and energy consumption increase in conventional and proposed hardware implementations.

Table 1 and Table 5 together summarize how the proposed SSQA accelerator diverges from prior SSA hardware [15]. Because the reference design is spin-parallel and limited to four-neighbor lattices, we benchmark both approaches on the G11–G13 instances that fit its topology, using identical cost functions and annealing schedules wherever possible. Due to the slow convergence characteristics of SSA compared to SSQA, the number of annealing steps for SSA was set to 90,000. In contrast, SSQA achieves comparable or slightly better average cut values using only 500 annealing steps. Moreover, the conventional hardware requires not only a significantly larger number of annealing steps but also the storage of intermediate spin states, resulting in a large memory footprint of 13.2 Mb BRAM. In contrast, the proposed SSQA hardware only needs to store the final replicas at $R = 20$, reducing the required BRAM size to just 32 kb, which corresponds to a 99.8% reduction in memory usage.

Table 6 presents a performance comparison between the proposed method and conventional annealing architectures from previous studies, using the G11 benchmark as the target graph. Both conventional methods adopt a spin-parallel architecture, which limits their applicability to graphs with only nearest-neighbor connections. In contrast, the proposed architecture employs a spin-serial structure, enabling the processing of fully connected graphs. Due to this architectural difference, the annealing latency of the proposed method is 12 ms, which is higher than that of the two conventional approaches. However, the proposed method achieves significant hardware resource savings. Compared to the HA-SSA architecture [15], it reduces energy consumption by 50%, the number of LUTs by 97%, the number of FFs by 88%, and the number of BRAM blocks by 70%. Compared to the IPAPT architecture [25], the number of LUTs and FFs are reduced by 93% and 92%, respectively.

Fig. 12 shows the mean cut values and annealing energy for the MAX-CUT benchmark G14. Conventional hardware architectures were limited to processing graphs with only four adjacent nodes. As a result, evaluations were restricted to benchmarks such as G11, G12, and G13 [15, 25]. In contrast, the proposed hardware is capable of handling fully connected graphs, which allows it to process more complex topologies like G14, where each node is connected to more than four others. Since conventional hardware cannot process such dense graphs, we conducted a performance comparison between the proposed SSQA algorithm implemented on GPU and the conventional SSA algorithm on GPU instead. The SSA algorithm runs for 10,000 annealing steps and the SSQA algorithms with $R = 20$ run for 500 steps. Compared to SSA (GPU) and SSQA (GPU), the proposed method achieved comparable average cut values while reducing the energy consumption by 99.998% and 99.992%, respectively.

5 SENSITIVITY ANALYSES AND DISCUSSION

5.1 Latency-area trade-off

Owing to the node-serial spin update, the present implementation requires 12.0 ms to solve the 800-spin G11 instance—longer than the 1 ms of the previous HA-SSA FPGA. Nevertheless, our design consumes only 20 % of the XC7Z045 fabric, yielding an *area-delay product (ADP)* of $ADP_{\text{serial}} = 0.199 \times 12.0 \text{ ms} = 2.39 \text{ ms}$. Note that area is $\max\{\text{LUT}\%, \text{FF}\%, \text{BRAM}\%\}$. In the proposed hardware, $A = 19.9\%$ (BRAM-dominated). For edge-class optimisers, an interaction latency of 50 ms is generally accepted [29]; hence the serial configuration already meets real-time constraints while cutting area—and thus cost and idle power—by more than 60 % compared with HA-SSA.

Because the datapath is fully pipelined, latency can be *linearly reduced* by instantiating p parallel spin engines. A ten-way parallel variant, for example, shortens latency to 1.2 ms while lifting resource utilisation to 54.8 %, resulting in $ADP_{p=10} = 0.648 \text{ ms}$ (3.7 \times lower than the serial design) and still remaining below the 80 % BRAM ceiling of HA-SSA. The constant energy per solve (1.1 mJ) stems from the proportional increase in power with p , implying that designers may trade silicon for speed without compromising battery life.

Further latency reductions could be achieved by (i) selectively parallelising high-degree spins, (ii) interleaving replica updates to hide memory latency, and (iii) sparsifying or quantising the weight matrix so that the BRAM footprint scales sub-linearly with problem size. Compression schemes such as run-length or delta encoding would release additional BRAM blocks, enabling graphs well beyond 10 000 spins to fit on mid-range FPGAs. These enhancements will broaden the applicability of the architecture to real-time machine-learning inference, embedded optimisation, and event-driven neuromorphic workloads.

Across the sweep of $N = 100$ to $N = 800$ spins in Fig. 10, LUT and FF usage vary by less than

Table 7: Qualitative comparison of FPGA-based annealing architectures

	[31]	[32]	[33]	This work
Hardware cost (LUTs/FFs)	Small	Large	Large	Small
Graph configuration	2D nearest-neighbor	Fully connected	Fully connected	Fully connected
Scheduling logic	Complex	Simple	Simple	Simple
Power consumption	Low	High	High	Low
Processing speed	High	High	Low	Middle
Energy efficiency	High	Low	Low	High

5%, confirming that the dual-BRAM delay line decouples logic cost from graph density. Power measurements follow the same trend, underscoring that scalability derives from the architectural changes rather than device-specific tuning.

5.2 Applicability to other combinatorial optimization problems

Beyond MAX-CUT, the SSQA algorithm itself has been validated on other combinatorial benchmarks. We apply the same replica-coupled update rule to traveling salesman (TSP) and graph isomorphism (GI) instances, demonstrating algorithm-level convergence on both domains [17]. In particular, their GI study shows that with $R = 25$ replicas SSQA sustains a 51% success probability at $N = 2,025$ nodes and cuts the time-to-solution (TTS) to 146 s, a 91.4% reduction relative to SSA’s 1,690 s TTS under the same cycle budget; SA requires 62,022 s for the same instance (423 \times slower). Even for $N = 2,500$, SSQA still converges in 405 s with 41% success while SSA fails to reach the optimum [17]. Because our FPGA bitstream implements the identical update rules and replica interactions, those GI and TSP instances—and any problem that admits an equivalent QUBO formulation [18]—can be executed by updating only the BRAM initialization files, without architectural changes.

The synthesizable SystemVerilog source code, host-side drivers, and Python reference implementation are available in our public repository [30]. The project includes Vivado 2023.2 configuration scripts, BRAM initialization files, and unit tests that mirror the benchmarks discussed above to aid reproducibility.

5.3 Comparison with Ising/QUBO annealers

Table 6 focuses on FPGA-class baselines, yet fully connected Ising/QUBO accelerators also exist in custom CMOS and quantum hardware. Fujitsu’s Digital Annealer [34] implements a massively parallel simulated annealer that solves dense QUBOs of up to 8,192 variables but requires datacenter-scale power budgets (>100 W) and proprietary cooling. Superconducting quantum annealers such as D-Wave Advantage [35] offer quantum tunneling and larger solution spaces but operate at milli-Kelvin temperatures and impose sparse Chimera/Pegasus connectivity, necessitating costly minor-embedding. Our FPGA-based p-bit engine instead targets sub-watt envelopes and natively supports arbitrary connectivity without embedding overhead.

As summarized in Table 7, among FPGA implementations the proposed architecture provides the lowest LUT/FF footprint while maintaining full connectivity. Resource-sharing [31] and chaotic Boltzmann machine [32] designs either forego dense graphs or sacrifice energy efficiency; the highly-parallel SQA system [33] attains massive scale but pays a 5–270 ms step latency (roughly 2.1×10^2 – 1.1×10^4 slower than our 24 μ s), even before considering power.

The contrast also clarifies the advantages and trade-offs of p-bit annealers. Unlike analog Ising machines that rely on continuous device dynamics, p-bit fabrics store probabilistic states digitally, making them resilient to fabrication variability and amenable to formal verification. Compared with QUBO-centric digital annealers, our architecture consumes less memory by streaming weights and storing only final replicas, at the expense of higher per-step latency. These properties make the proposed design attractive for embedded optimisation workloads where energy and programmability outweigh absolute throughput.

6 Conclusion

We presented an energy-efficient hardware architecture for fully connected simulated annealing, combining a quantum-inspired SSQA algorithm with a spin-serial/replica-parallel design and a dual-BRAM delay scheme. This architecture addresses both connectivity and scalability challenges in conventional p-bit-based annealing hardware. Unlike nearest-neighbor-limited or shift-register-based approaches, our design supports fully connected graphs while maintaining nearly constant LUT and FF usage as the number of spins increases, thanks to the separation of logic and memory enabled by the dual-BRAM scheme. Evaluation on the G11 instance from the G-set benchmark confirmed significant resource and energy efficiency, achieving over 50% reduction in energy consumption, 97% reduction in logic resource usage, and a 70% reduction in BRAM consumption, without compromising solution quality. These results demonstrate the feasibility of scalable, quantum-inspired optimization hardware on modern FPGAs.

Future work includes reducing BRAM usage through sparsification, quantization, or compression of the weight matrix, as well as extending support to other combinatorial problems such as graph coloring and the traveling salesman problem. Additionally, integration with emerging memory devices such as MRAM or spintronic-based p-bits will be explored to further improve efficiency and practicality for real-world applications.

References

- [1] K. Camsari, R. Faria, B. Sutton, and S. Datta, “Stochastic p-bits for invertible logic,” *Physical Review X*, vol. 7, July 2017.
- [2] W. A. Borders, A. Z. Pervaiz, S. Fukami, K. Y. Camsari, H. Ohno, and S. Datta, “Integer factorization using stochastic magnetic tunnel junctions,” *Nature*, vol. 573, no. 7774, pp. 390–393, 2019. [Online]. Available: <https://doi.org/10.1038/s41586-019-1557-9>
- [3] K. Hayakawa, S. Kanai, T. Funatsu, J. Igarashi, B. Jinnai, W. A. Borders, H. Ohno, and S. Fukami, “Nanosecond random telegraph noise in in-plane magnetic tunnel junctions,” *Phys. Rev. Lett.*, vol. 126, p. 117202, Mar 2021. [Online]. Available: <https://link.aps.org/doi/10.1103/PhysRevLett.126.117202>
- [4] C. Safranski, J. Kaiser, P. Trouilloud, P. Hashemi, G. Hu, and J. Sun, “Demonstration of nanosecond operation in stochastic magnetic tunnel junctions.” *Nano Lett.*, vol. 21, pp. 2040–2045, Mar 2021.
- [5] G. E. Hinton, T. J. Sejnowski, and D. H. Ackley, “Boltzmann machines: Constraint satisfaction networks that learn,” Department of Computer Science, Carnegie-Mellon University, Tech. Rep. CMU-CS-84-119, 1984.

- [6] N. Onizawa, S. C. Smithson, B. H. Meyer, W. J. Gross, and T. Hanyu, “In-hardware training chip based on cmos invertible logic for machine learning,” *IEEE Transactions on Circuits and Systems I: Regular Papers*, vol. 67, no. 5, pp. 1541–1550, May 2020.
- [7] J. Kaiser, W. A. Borders, K. Y. Camsari, S. Fukami, H. Ohno, and S. Datta, “Hardware-aware in situ learning based on stochastic magnetic tunnel junctions,” *Phys. Rev. Appl.*, vol. 17, p. 014016, Jan 2022. [Online]. Available: <https://link.aps.org/doi/10.1103/PhysRevApplied.17.014016>
- [8] N. A. Aadit, A. Grimaldi, M. Carpentieri, L. Theogarajan, J. M. Martinis, G. Finocchio, and K. Y. Camsari, “Massively parallel probabilistic computing with sparse ising machines,” *Nature Electronics*, vol. 5, no. 7, pp. 460–468, 2022. [Online]. Available: <https://doi.org/10.1038/s41928-022-00774-2>
- [9] K. Y. Camsari, B. M. Sutton, and S. Datta, “p-bits for probabilistic spin logic,” *Applied Physics Reviews*, vol. 6, p. 011305, 2019.
- [10] N. Onizawa and T. Hanyu, “Enhanced convergence in p-bit based simulated annealing with partial deactivation for large-scale combinatorial optimization problems,” *Scientific Reports*, vol. 14, no. 1, p. 1339, 2024. [Online]. Available: <https://doi.org/10.1038/s41598-024-51639-x>
- [11] B. R. Gaines, “Stochastic computing systems,” *Adv. Inf. Syst. Sci. Plenum*, vol. 2, no. 2, pp. 37–172, 1969.
- [12] B. D. Brown and H. C. Card, “Stochastic neural computation. I. computational elements,” *IEEE Transactions on Computers*, vol. 50, no. 9, pp. 891–905, Sep. 2001.
- [13] V. C. Gaudet and W. J. Gross, *Stochastic Computing: Techniques and Applications*. Springer International Publishing, 2019.
- [14] N. Onizawa, K. Katsuki, D. Shin, W. J. Gross, and T. Hanyu, “Fast-converging simulated annealing for ising models based on integral stochastic computing,” *IEEE Transactions on Neural Networks and Learning Systems*, vol. 34, no. 12, pp. 10 999–11 005, 2023.
- [15] D. Shin, N. Onizawa, W. J. Gross, and T. Hanyu, “Memory-efficient fpga implementation of stochastic simulated annealing,” *IEEE Journal on Emerging and Selected Topics in Circuits and Systems*, vol. 13, no. 1, pp. 108–118, 2023.
- [16] T. Kubuta, D. Shin, N. Onizawa, and T. Hanyu, “Stochastic implementation of simulated quantum annealing on pynq,” in *2023 International Conference on Field Programmable Technology (ICFPT)*, 2023, pp. 274–275.
- [17] N. Onizawa, R. Sasaki, D. Shin, W. J. Gross, and T. Hanyu, “Stochastic simulated quantum annealing for fast solution of combinatorial optimization problems,” *IEEE Access*, vol. 12, pp. 102 050–102 060, 2024.
- [18] A. Lucas, “Ising formulations of many NP problems,” *Frontiers in Physics*, vol. 2, p. 5, 2014. [Online]. Available: <https://www.frontiersin.org/article/10.3389/fphy.2014.00005>
- [19] V. C. Gaudet and A. C. Rapley, “Iterative decoding using stochastic computation,” *Electronics Letters*, vol. 39, no. 3, pp. 299 – 301, Feb. 2003.

[20] P. Li, D. J. Lilja, W. Qian, K. Bazargan, and M. D. Riedel, “Computation on stochastic bit streams digital image processing case studies,” *IEEE Transactions on Very Large Scale Integration (VLSI) Systems*, vol. 22, no. 3, pp. 449–462, Mar. 2014.

[21] Y. Liu and K. K. Parhi, “Architectures for recursive digital filters using stochastic computing,” *IEEE Transactions on Signal Processing*, vol. 64, no. 14, pp. 3705–3718, July 2016.

[22] A. Ardakani, F. Leduc-Primeau, N. Onizawa, T. Hanyu, and W. J. Gross, “VLSI implementation of deep neural network using integral stochastic computing,” *IEEE Transactions on Very Large Scale Integration (VLSI) Systems*, vol. 25, no. 10, pp. 2588–2599, Oct. 2017.

[23] M. Suzuki, “Relationship between d-Dimensional Quantal Spin Systems and (d+1)-Dimensional Ising Systems: Equivalence, Critical Exponents and Systematic Approximants of the Partition Function and Spin Correlations,” *Progress of Theoretical Physics*, vol. 56, no. 5, pp. 1454–1469, 11 1976. [Online]. Available: <https://doi.org/10.1143/PTP.56.1454>

[24] G. E. Santoro, R. Martonvák, E. Tosatti, and R. Car, “Theory of quantum annealing of an ising spin glass,” *Science*, vol. 295, no. 5564, pp. 2427–2430, mar 2002. [Online]. Available: <https://doi.org/10.1126%2Fscience.1068774>

[25] H. Gyoten, M. Hiromoto, and T. Sato, “Enhancing the solution quality of hardware ising-model solver via parallel tempering,” in *Proceedings of the International Conference on Computer-Aided Design*, ser. ICCAD ’18. New York, NY, USA: Association for Computing Machinery, 2018. [Online]. Available: <https://doi.org/10.1145/3240765.3240806>

[26] S. Vigna, “Further scramblings of Marsaglia’s xorshift generators,” *Journal of Computational and Applied Mathematics*, vol. 315, no. Supplement C, pp. 175–181, 2017.

[27] A. Klöckner, N. Pinto, Y. Lee, B. Catanzaro, P. Ivanov, and A. Fasih, “Pycuda: GPU run-time code generation for high-performance computing,” *CoRR*, vol. abs/0911.3456, 2009. [Online]. Available: <http://arxiv.org/abs/0911.3456>

[28] Y. Ye, “Computational optimization laboratory,” 1999. [Online]. Available: <http://web.stanford.edu/~yyye/Col.htm>

[29] J. Martens, T. Franke, N. Rauh, and J. F. Krems, “Effects of low-range latency on performance and perception in a virtual, unstable second-order control task,” *Quality and User Experience*, vol. 3, no. 10, pp. 1–21, 2018.

[30] N. Onizawa, T. Kubuta, D. Shin, and T. Hanyu, “SSQA FPGA design repository,” https://github.com/nonizawa/SSQA_FPGA, 2025, accessed: 2025-10-27.

[31] C. Yoshimura, M. Hayashi, T. Okuyama, and M. Yamaoka, “Implementation and evaluation of FPGA-based annealing processor for ising model by use of resource sharing,” *International Journal of Networking and Computing*, vol. 7, no. 2, pp. 154–172, 2017.

[32] K. Yoshioka, Y. Katori, Y. Tanaka, O. Nomura, T. Morie, and H. Tamukoh, “FPGA implementation of a chaotic boltzmann machine annealer,” in *Proceedings of the International Joint Conference on Neural Networks (IJCNN)*, 2023, pp. 1–8.

[33] H. M. Waidyasoorya and M. Hariyama, “Highly-parallel FPGA accelerator for simulated quantum annealing,” *IEEE Transactions on Emerging Topics in Computing*, vol. 9, no. 4, pp. 2019–2029, 2021.

- [34] M. Aramon, G. Rosenberg, E. Valiante, T. Miyazawa, H. Tamura, and H. G. Katzgraber, “Physics-inspired optimization for quadratic unconstrained problems using a digital annealer,” *Frontiers in Physics*, vol. 7, 2019. [Online]. Available: <https://www.frontiersin.org/articles/10.3389/fphy.2019.00048>
- [35] S. Boixo, T. F. Rønnow, S. V. Isakov, Z. Wang, D. Wecker, D. A. Lidar, J. M. Martinis, and M. Troyer, “Evidence for quantum annealing with more than one hundred qubits,” *Nature Physics*, vol. 10, no. 3, pp. 218–224, 2014. [Online]. Available: <https://doi.org/10.1038/nphys2900>

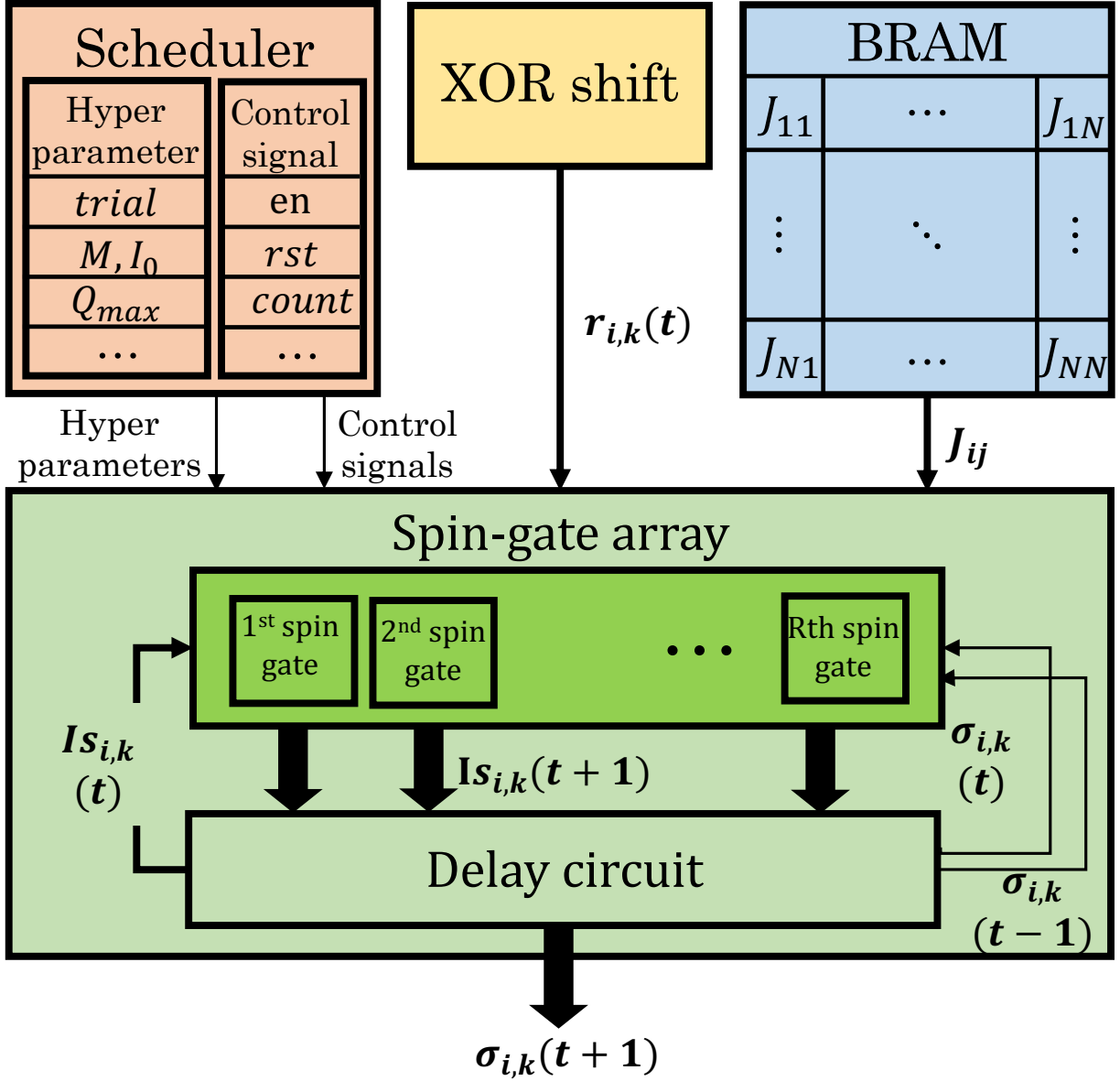


Figure 4: Spin-serial and replica-parallel architecture of the proposed SSQA hardware. The design comprises R spin gate circuits that are reused N times to compute a total of $R \times N$ spins. The spin-serial structure reduces wiring complexity, while the replica-parallel structure allows concurrent access to shared weights, enabling efficient and scalable computation for fully connected graphs.

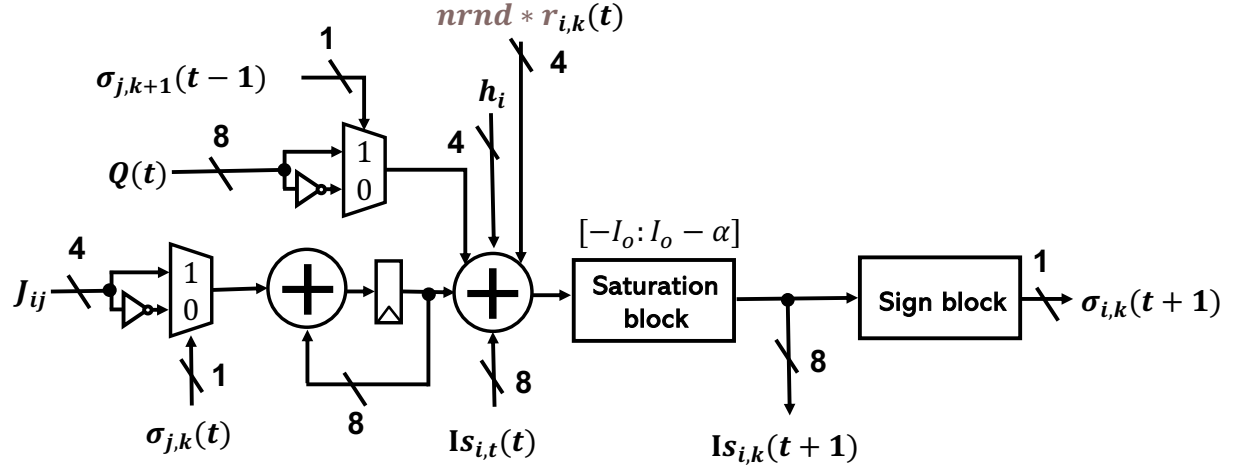


Figure 5: Spin-serial spin gate circuit implementing the update rule in Eq. (6). At each clock cycle, the output of one spin and the corresponding weight J_{ij} are sequentially read from BRAM to compute spin interactions. This time-multiplexed design allows hardware resource reduction while supporting arbitrary spin connectivity.

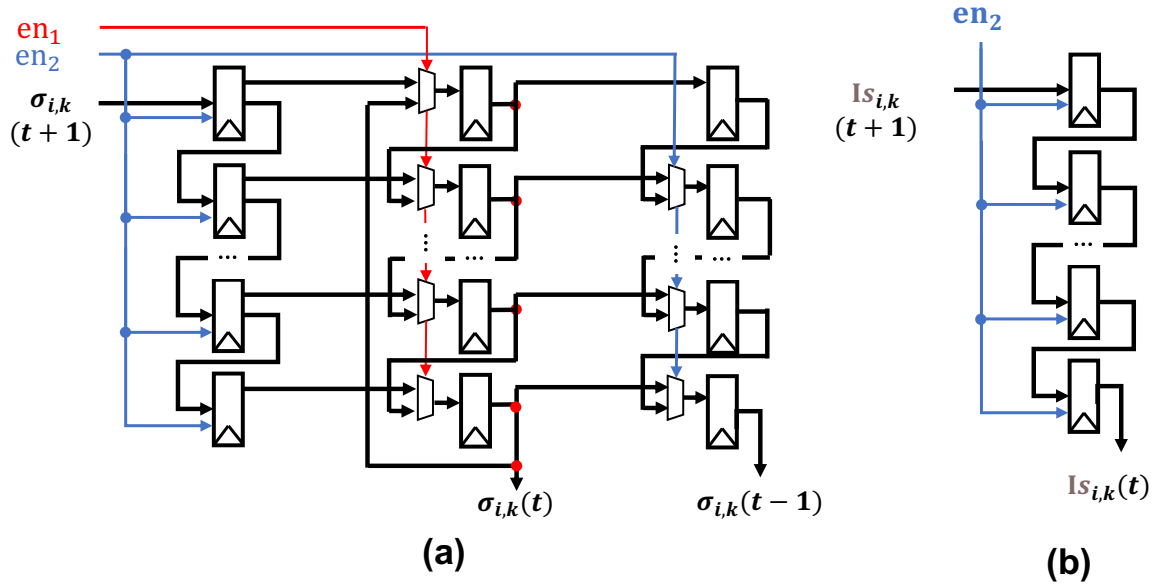
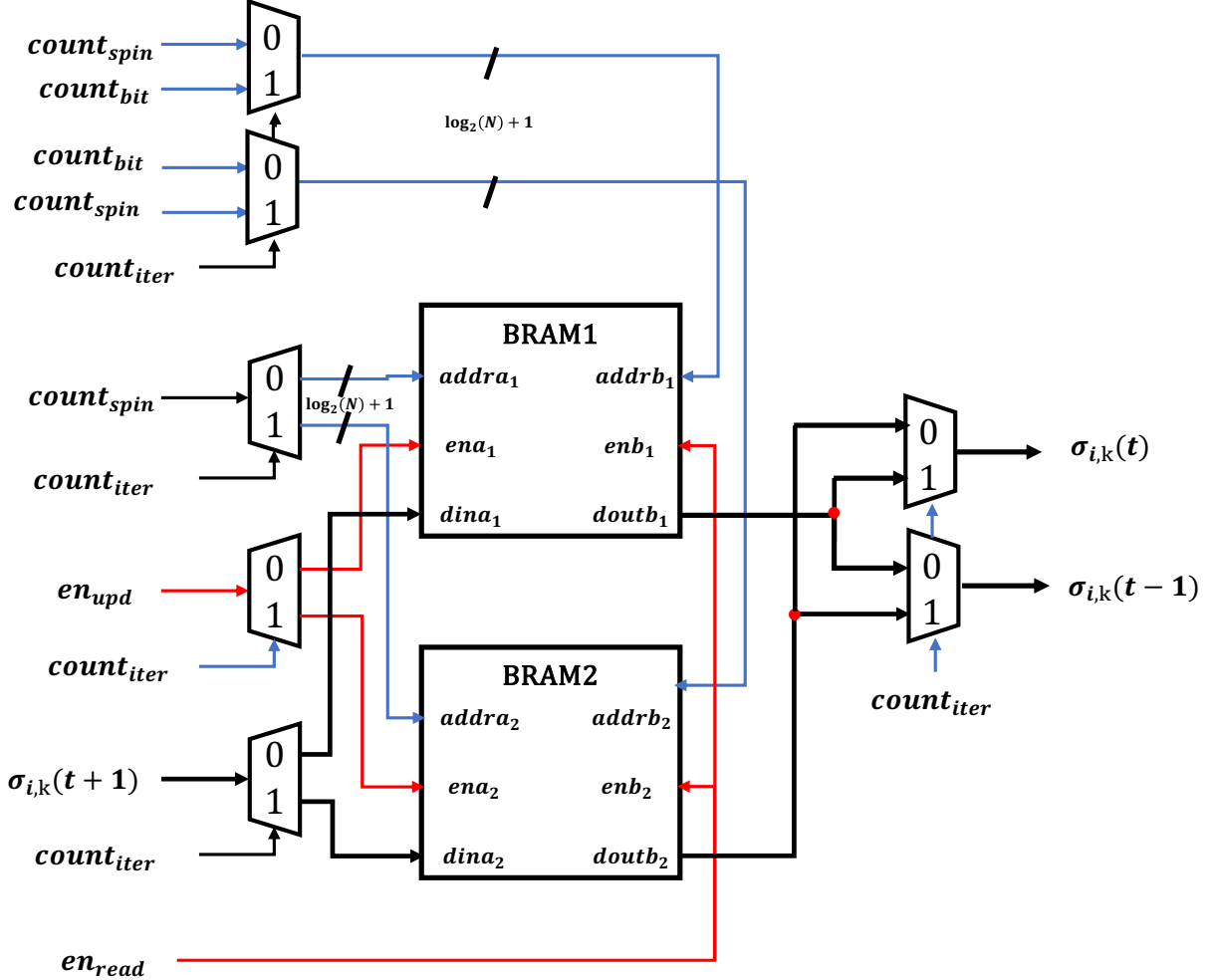
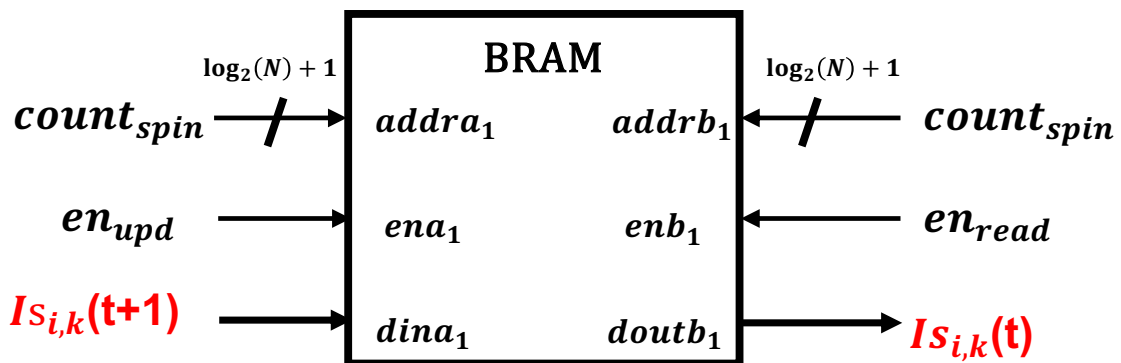


Figure 6: Shift register-based delay circuits used in the k -th replicated spin gate: (a) stores spin states $\sigma_{i,k}$ over three consecutive annealing steps, and (b) stores the corresponding saturated internal signals $Is_{i,k}$. While straightforward to implement, this design scales poorly with the number of spins due to increased register usage and signal fan-out.



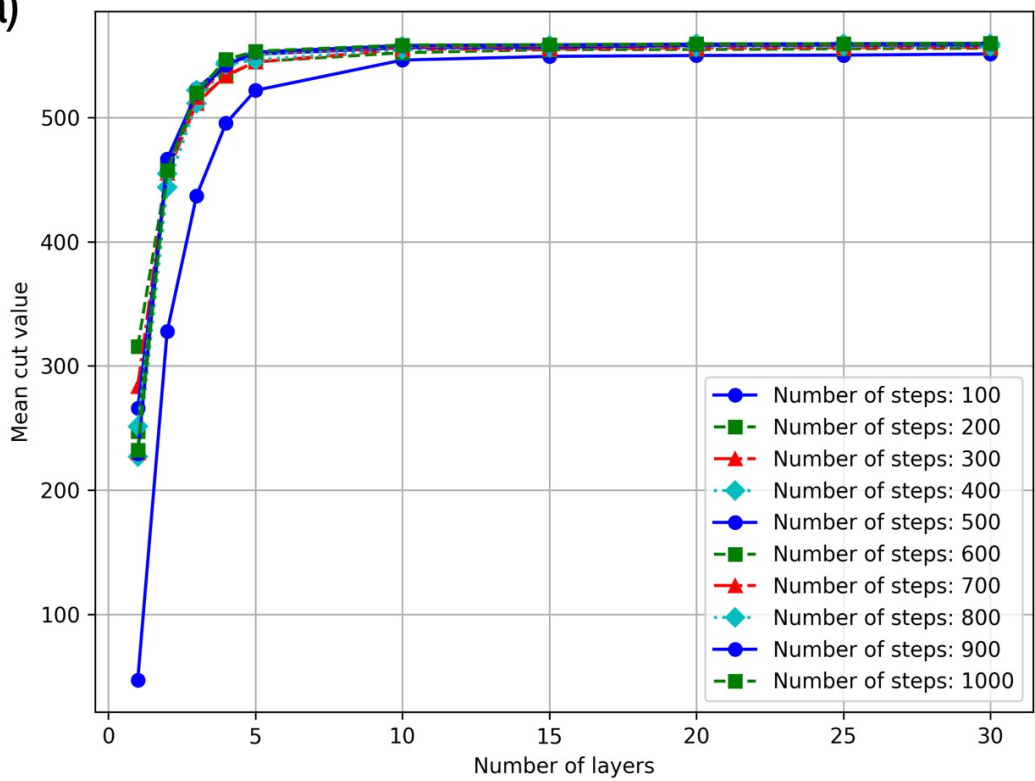
(a)



(b)

Figure 7: Dual BRAM-based delay circuits for the k -th replicated spin gate: (a) handles spin states $\sigma_{i,k}$, and (b) handles saturated internal signals $Is_{i,k}$. Two BRAMs alternate read/write operations across annealing steps, enabling delay of one and two time steps. This structure alleviates scalability issues seen in shift register designs by centralizing memory access and minimizing control signal fan-out.

(a)



(b)

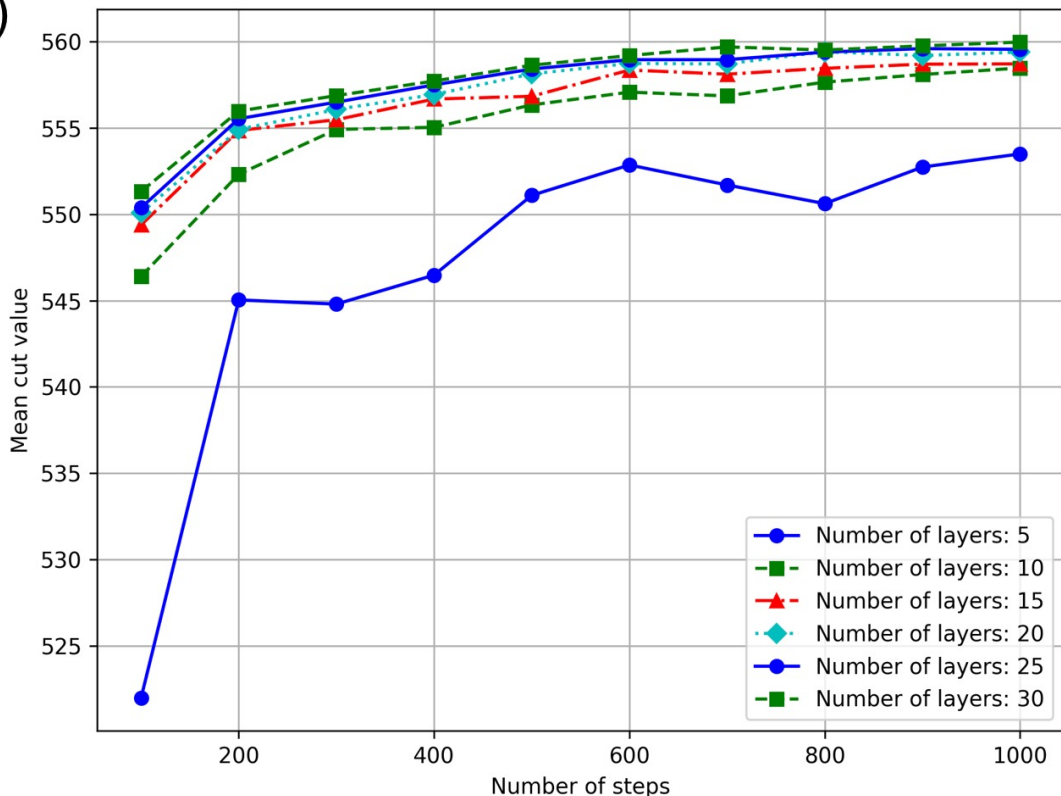


Figure 8: Evaluation of the SSQA algorithm for the G11 instance: (a) average cut value versus the number of layers R , showing performance saturation beyond $R = 15$; (b) average cut value versus number of simulation steps for different R values, with saturation observed for $R \geq 20$.

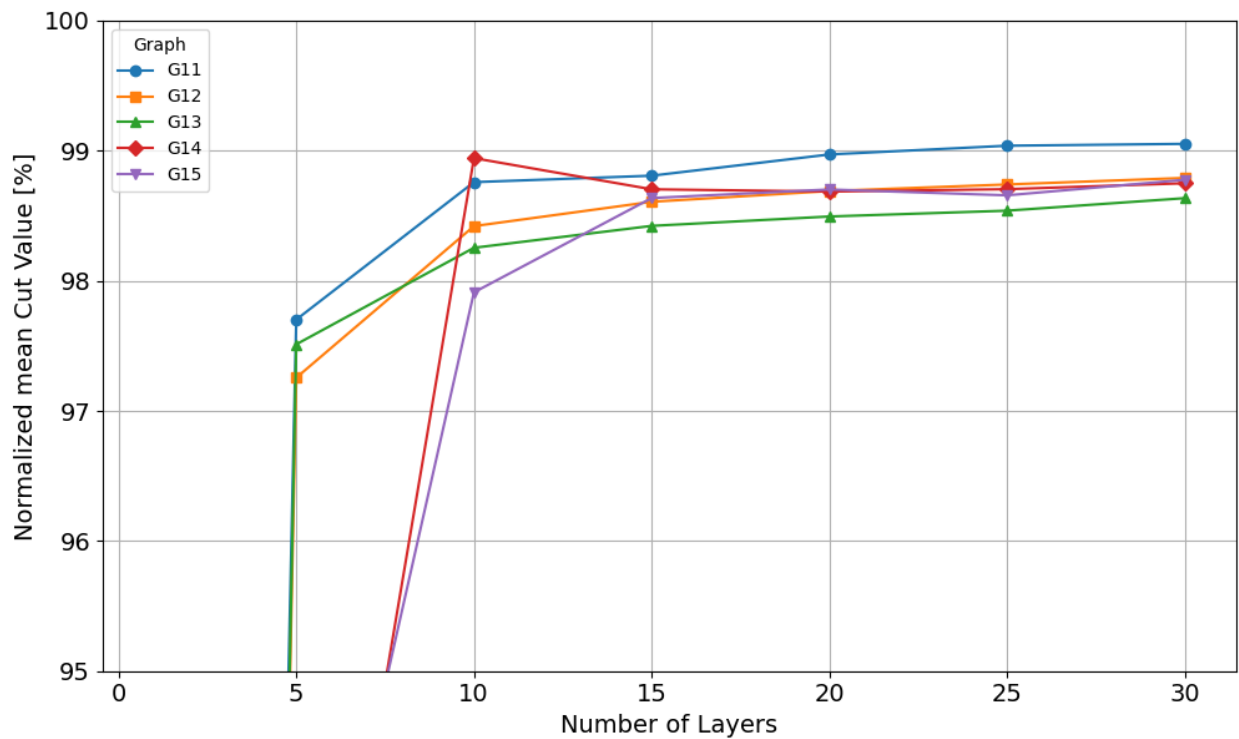


Figure 9: Normalized mean cut value vs. number of layers (R) in SSQA. Normalized mean cut values nearly saturate at $R = 20$.

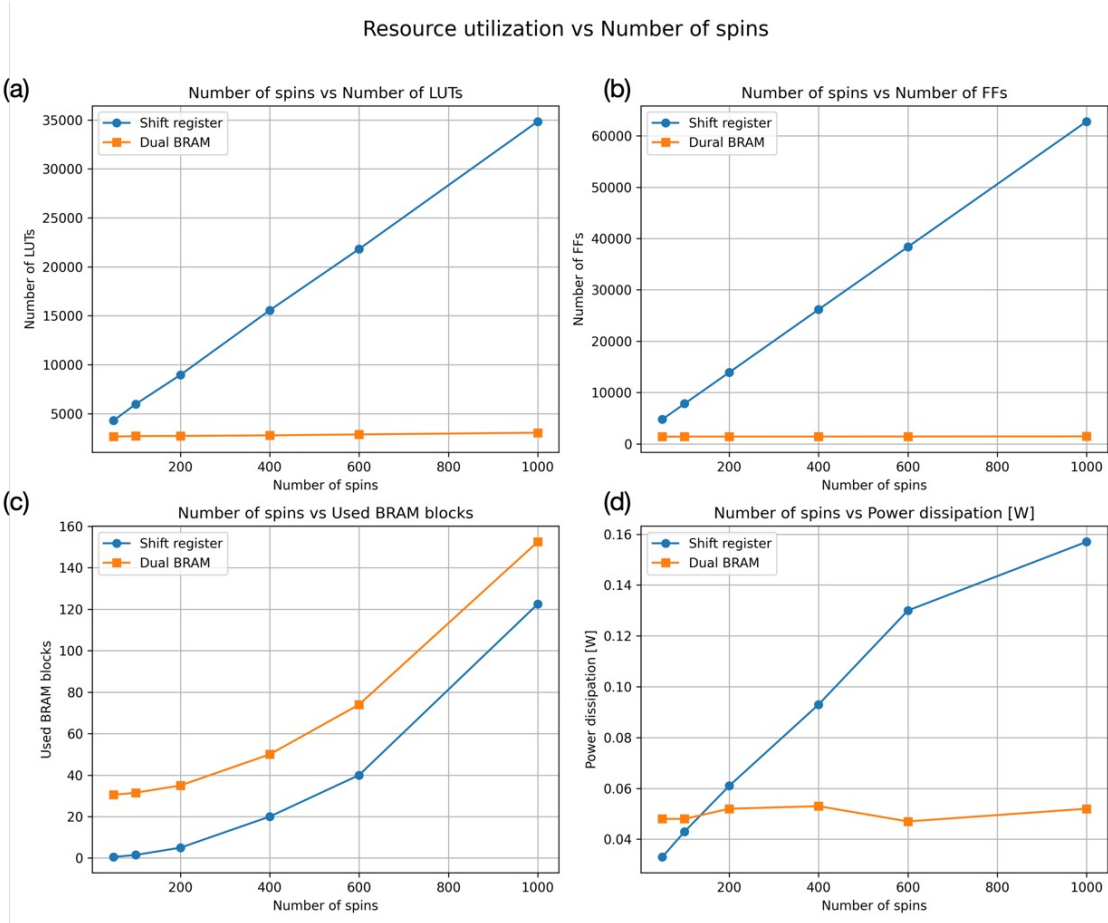


Figure 10: Comparison of resource usage and power consumption between shift register-based and dual-BRAM-based SSQA hardware implementations: (a) LUT usage remains constant in dual-BRAM but grows with spin count in shift-register design; (b) FF usage increases linearly only in the shift-register case; (c) BRAM usage increases with N^2 , with higher overhead in dual-BRAM due to delay circuit storage; (d) power consumption scales with spin count in the shift-register design but remains stable in dual-BRAM implementation.

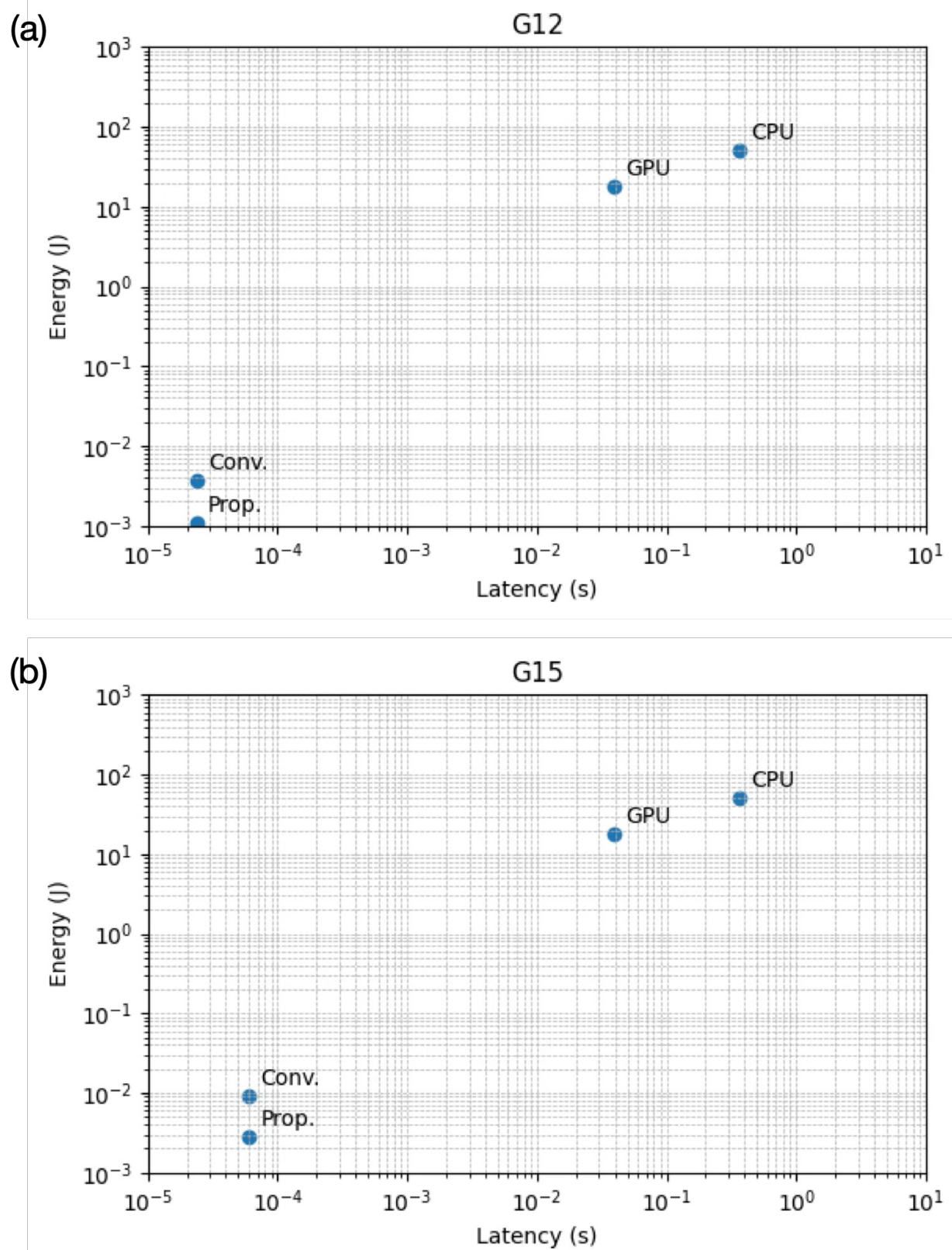
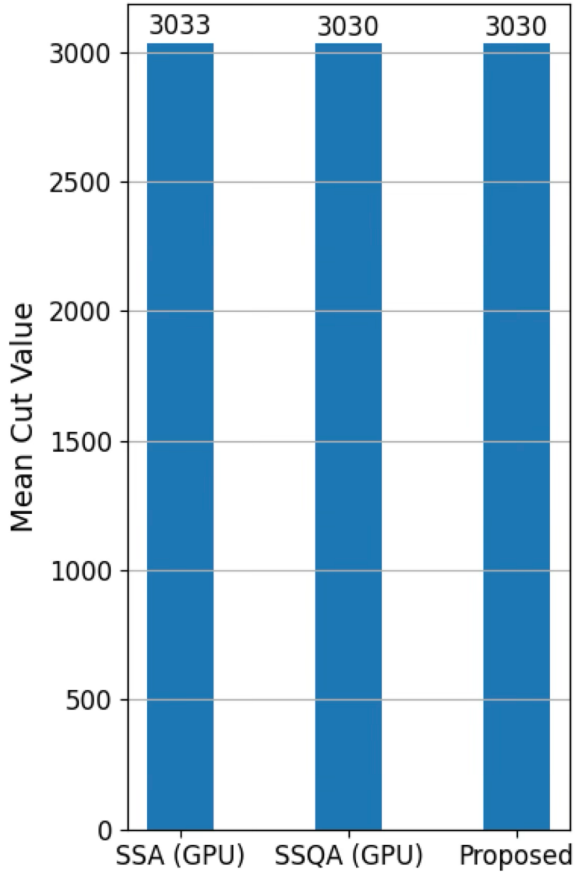
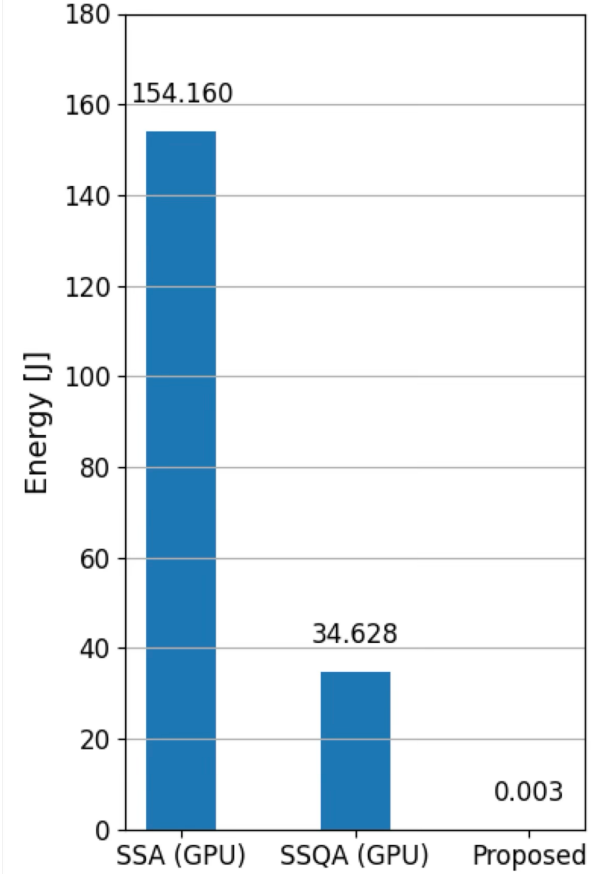


Figure 11: Energy-latency trade-off in SSQA implementations for two graph instances (G12 and G15), each executed for 500 annealing steps. (a) and (b) show the results for G12 and G15, respectively. The proposed dual-BRAM-based hardware demonstrates significantly lower energy consumption and latency compared to CPU and GPU implementations. Due to the higher connectivity and larger number of steps in G15, both latency and energy increase for the FPGA implementations.



(a)



(b)

Figure 12: Comparisons of mean cut value and energy for G14: (a) mean cut values obtained for 100 trials and (b) annealing energy.